Minimum-Reactive-Power Scheme of Dual Active Bridge DC-DC Converter With 3-Level Modulated Phase-Shift Control

Haochen Shi, Huiqing Wen, *Member, IEEE,* Jie Chen, Yihua Hu, *Senior Member, IEEE,*
Lin Jiang, *Member, IEEE,* Guipeng Chen, *Student Member, IEEE*

***Abstract*—This paper presents a novel reactive power minimization method under 3-level modulated phase-shift control to improve the efficiency for a wide operation condition. Firstly, in order to unify all operation modes, a mathematic model of the DAB converter with 3-level modulated phase-shift control by a harmonic analysis method is obtained. Then, the detailed analysis of the odd-order harmonic components of the active and reactive varied with the multiple control dimensions is presented. The soft-switching boundaries with respect to the voltage ratio and unified active power are specified. On this basis, a novel optimal 3-level phase-shift control (OPS) strategy for minimizing reactive power is proposed. Experimental results about reactive power and operation efficiency among the proposed OPS method and other methods are compared to verify the effectiveness of OPS algorithm.**

***Index Term*—dual active bridge, phase shift, 3-level modulated control, reactive power, harmonic analysis, zero voltage switching(ZVS)**

I. INTRODUCTION

THE dual-active-bridge dc-dc converter has shown significant advantages in the future distributed power system, including high power density, bidirectional power flow ability, current isolation and soft-switching ability [1-3]. The most commonly-used control strategy is called the single-phase-shift (SPS) or conventional-phase-shift control (CPS) [4], which only controls the single phase shift between two sides of the transformer. Thus, the transmission power monotonously increases with the phase-shift angle. However, the reactive power, especially the backflow power will be quite significant when the primary-side voltage and the secondary-side voltage are mismatched. Besides, the soft-switching region becomes narrow with this control under the mismatched condition [5]. Furthermore, it will result in high root-mean-square (RMS) current and hard switching which lead to high conduction losses and switching losses, and finally seriously affect the overall transmission efficiency [4-13].

In order to overcome those drawbacks in the traditional SPS control, the 3-level phase-shift modulated method is proposed [14-23]. Compared with the SPS control, 3-level phase-shift modulated strategy can gain an addition PWM control freedom by adjusting an extra inner phase-shift angle between two bridge arms, which allows a 3-level PWM ac voltage output in each bridge instead of the traditional square-wave ac voltage output. Thus, it can dramatically improve the control flexibility and simultaneously ensure soft-switching region extension and backflow power reduction [24]. According to different inner phase shift modes, it can be divided into three categories: the dual-phase-shift (DPS) control, which is achieved by adding a same inner phase shift angle on both sides of the bridge for ensuring symmetric 3-level PWM wave output and reducing backflow power [14-16]. The second category is the extended-phase-shift (EPS) control, which has a single-bridge-side inner phase shift angle [17-20]. The third type is the triple-phase-shift (TPS) control, which has two double-bridge-side independent inner phase shift angles, while the SPS, DPS and EPS control can be regarded as a special case of the TPS control [21-23]. Both EPS and TPS output are the asymmetric 3-level PWM waveforms.

In order to further reduce power losses, originated from the principle of 3-level modulated phase-shift control, some advanced control strategies are proposed. For instance, in order to reduce the conduction loss, an optimization control method is proposed and mainly focused on the nonactive current minimization [24]. The current-stress-optimized (CSO) algorithms are proposed to reduce conduction loss and the RMS current stress of inductor is treated as the optimization objective [25-27]. A PI-based current sensorless control is discussed in [27], which can simplify the control complexity and remove required current and voltage sensors. An efficiency optimization algorithm is presented in [28] with the aim to minimize switching losses and conduction losses. Those optimization control strategy can significantly improve efficiency by adjusting optimum operation points for different operation modes, but the asymmetric structure makes the control implementation extremely complicated, furthermore, the boundaries for various modes are hard to determine.

Conventionally, the linear piecewise time domain model is used in the theoretical analysis of the 3-level phase shift method [4-29]. However, it can't be expressed by a single universal expression because of the linear mathematic model for inductor current under different operation states and the changing load conditions in the time domain analysis. It also needs to specify the boundaries for all operation modes. Furthermore, detailed operations modes under different conditions in terms of load and voltage conversion ratio must be separately discussed, which will significantly increase the implementation difficulty. According to the simplified ideal inductive model of DAB converter, the linear inductor current can be approximately

obtained at [30]. However, the equivalent model for the coupling inductor or transformer is nonlinear, which make the algorithm implementation extremely difficult since the integration operations of state equations are required [31-33].

How to determine the optimal operation point requires a lot of complicated calculations due to the complexity of the piecewise time domain expression. Furthermore, the obtained result is also a piecewise time domain function which is varying with different load and voltage conversion condition [24-36]. The efficiency and current stress optimization algorithms have been discussed in [25] and [28], which shows that the expressions for optimal points are too complex for online calculations in the microchip. It requires an offline parameter calculation to switch the optimal function and adapt different operation states. Another problem for the linear piecewise model is the non-sinusoidal 3-level PWM wave outputs since their active and reactive power are hard to determine. Furthermore, these optimization methods simply take the input-side backflow power or current stress as the reactive power, which is not accurate and ultimately affects the effectiveness of these methods.

In this paper, a universal expression for 3-level modulated phase-shift control by a harmonic analysis method is proposed to overcome weaknesses of the tradition linear piecewise time-domain model. In the harmonic analytical model, 3-level PWM wave for each bridge under TPS control can be expressed in the frequency domain as harmonic series forms. Then, the inductor current can be calculated from the second port network parameters and three independent phase shift angles. After that, the expressions of active and reactive power with harmonic components can be obtained. Based on that, the effect of variable order harmonic components on the soft-switching region, active and reactive power will be discussed. Then, an optimal reactive power minimization algorithm under 3-level modulated control is proposed. Both the theoretical analysis and experimental results are presented.

II. HARMONIC SERIES ANALYSIS OF 3-LEVEL PHASE-SHIFT MODULATED CONTROL

A. Typical 3-level modulation structure

The DAB converter illustrated in Fig. 1 can be analyzed as a two-port network. The V_{B1} is the AC voltage of primary bridge and V_{B2} is the AC voltage of the secondary bridge refers to the primary side. The network Y represents the network parameter for the two-port network. In this paper, the network Y is considered as an ideal inductive network.

Typical waveforms of 3-level phase-shift modulation are shown in Fig. 2. The 3-level waveform in each bridge is produced by setting an inner phase shift of two-switch pair in one bridge elaborately. In Fig. 2, the angle α and β are defined as the inner phase angles for V_{B1} and V_{B2}, while i_1 and i_2 represent the current of each bridge. The phase shift angle between two bridges is named as the outer phase shift angle θ. Thus, the SPS control can be seen as a special case

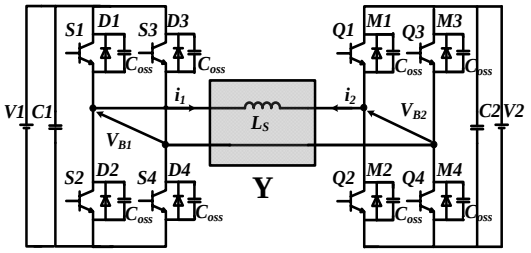

Fig. 1. Topology of DAB converter

of the 3-level phase shift modulation when $\alpha=\beta=0$. The benefit of the 3-level phase-shift modulation is the capability in reducing the undesirable circulating current flowing within each bridge. For example, the inductor current flowing path during t_0 and t_1 is illustrated in Fig.3. At this period, the inductor current i_1 is negative, while D_1, S_3 on the primary side and M_2, M_3 on the secondary side are on. Thus, on the secondary bridge, the inductor current is transferred from inductor to output port V_2 by diode M_2 and M_3. However, on the primary bridge, the inductor current is circulating inside bridge through S_3 and D_1 instead of flowing back to the source V_1. So the circulating current or backflow current during this period can be reduced in order to minimize the conduction loss.

In order to simplify the universal expression, the 3-level wave should show good feature of symmetric structure [13]. In order to achieve that, the starting point is set as "$i(t_0)=\alpha/2$", which allow a symmetric structure of 3-level wave in half cycle [37]. Then, the phase shift between two 3-level waves is δ, which is the angle between the central points of each pulse wave. It indicates the influence of the inner phase shift α and β, as well as the outer phase shift θ. The relationship among the central point phase shift angle δ with inner and outer phase shifts can be expressed as "$\delta=\theta+(\alpha-\beta)/2$". Thus, the 3-level wave modulation could be described as a symmetric structure, which will significantly reduce the complexity of calculation [38].

B. Harmonic Series Form of Voltage and Current

According to the Fourier series, any periodic function can be transferred into the sum of sine and cosine functions. So the 3-level square wave can be divided into a combination of series odd-order harmonics components by simple sine and cosine functions. The AC link primary and secondary side voltage V_{B1} and V_{B2} can be expressed as:

$$\begin{cases} V_{B1}=\sum\limits_{n=1,3,5,\ldots}\dfrac{4V_1}{n\pi}\cos(n\alpha/2) \\ V_{B2}=\sum\limits_{n=1,2,3,\ldots}\dfrac{4V_2}{n\pi}\cos(n\beta/2)\left[\cos(\delta)-j\sin(\delta)\right] \end{cases} \quad (1)$$

In Fig. 1, V_{B1} and V_{B2} can be regarded as terminal voltages of a simple two-port network, which includes the equivalent model of leakage inductor and auxiliary inductor as well as the transformer. The expression can be obtained as:

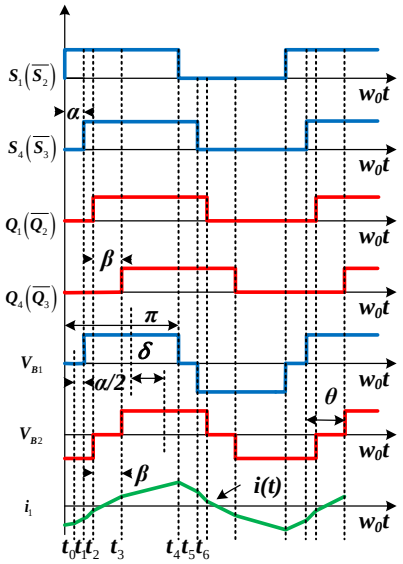

Fig. 2. Typical waveforms of the 3-level modulated phase shift control.

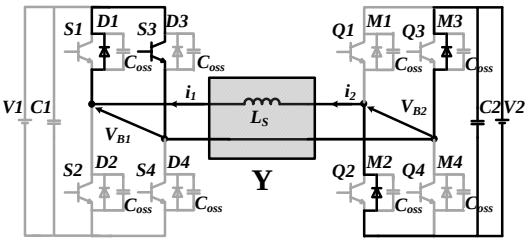

Fig. 3. The inductor current flowing path during t_0 and t_1.

$$\begin{bmatrix} I_1 \\ I_2 \end{bmatrix} = \begin{bmatrix} Y_{11} & Y_{12} \\ Y_{21} & Y_{22} \end{bmatrix} \begin{bmatrix} V_{B1} \\ V_{B2} \end{bmatrix} \tag{2}$$

where $[Y]$ is the admittance matrix of the Network Y. Considering the network Y is an ideal inductive network, I_1 can be calculated from (1)-(2) as:

$$I_1 = \sum_{n=1,3,5,..} \frac{4}{n^2 \pi \omega_0 L} \sqrt{A^2+B^2} \left[\cos\left(\arctan\frac{A}{B} \right) + j \sin\left(\arctan\frac{A}{B} \right) \right] \tag{3}$$

where $\omega_0 = 2\pi f_{sw}$, and

$$\begin{cases} A = V_2 \cos(n\beta/2)\cos(n\delta) - V_1 \cos(n\alpha/2) \\ B = V_2 \cos(n\beta/2)\sin(n\delta) \end{cases} \tag{4}$$

With the (1)-(4), the AC link voltage and inductor current in the different operation conditions with the 3-level modulated phase-shift method can be expressed by a universal mathematical model, which is the combination of odd-order harmonics components. Thus, compared with the DAB mathematical model with the traditional piecewise expression, this complexity of this universal model has been significantly simplified.

C. Harmonic Series Forms of Active Power

The active power for DAB can be expressed as:

$$P = VI\cos(\varphi) \tag{5}$$

where the power factor $\cos(\varphi)$ is used to indicate the phase differences between the voltage and current. Since both voltage and current are in the form of harmonic series, the power factor can be divided into two situations: 1) For the current and voltage with the same order harmonic component, the power factor is followed by (5). 2) For the voltage and current with different order harmonic components, the active power is equal to 0 due to the orthogonality of trigonometric function. So we have

$$\begin{cases} \cos(\varphi)_{m=n} = \cos(-\arctan\frac{A}{B}) \\ \cos(\varphi)_{m\neq n} = 0 \end{cases} \tag{6}$$

Taking this condition into the (1)-(6), we have

$$\begin{aligned} P &= \sum_{n=1,3,5,..} \frac{8V_1\sqrt{A^2+B^2}}{n^3\pi^2\omega_0 L} \cos(n\alpha/2)\cos\left(-\arctan\frac{A}{B}\right) \\ &= \sum_{n=1,3,5,..} \frac{8V_1V_2}{n^3\pi^2\omega_0 L} \cos(n\alpha/2)\cos(n\beta/2)\sin(n\delta) \end{aligned} \tag{7}$$

The active power can be normalized by the unified power $P_N = V_1 * V_2/(8 f_s * L)$, so the normalized power T can be gained as

$$T = \sum_{n=1,3,5,..} \frac{32}{n^3\pi^3} \cos(n\alpha/2)\cos(n\beta/2)\sin(n\delta) \tag{8}$$

Fig. 4(a) illustrates the relationship of the unified active power in different order components along with the central point angle δ. T is the overall unified active power, T_1, T_3, T_5 are the fundamental, third order and fifth order components of the unified active power. The active power in all order components is axis symmetry around $\delta = \pi/2$. It shows that the fundamental components of the active power are the majority part of the active power. It confirms the analysis result of the active power in the piecewise time domain model. It proves that the fundamental components of active power can be used to represent the active power with a negligible error.

D. Harmonic Series Forms of Reactive Power

Due to the phase difference between the AC voltage and current, the DAB converter also contains a reactive power. The reactive power of the DAB can be expressed as:

$$Q = VI\sin(\varphi) \tag{9}$$

Compared with the active power, the reactive power is not only occurred between the same order voltage and current but also caused by the different order components. So the reactive power can be derived as:

$$\begin{aligned} Q_{m=n} &= \sum_{n=1,3,5,..} \frac{8V_1\sqrt{A^2+B^2}}{n^3\pi^2\omega_0 L} \cos(n\alpha/2)\sin\left(-\arctan\frac{A}{B}\right) \\ &= \sum_{n=1,3,5,..} \frac{8V_1}{n^3\pi^2\omega_0 L} \Big[V_1 \cos^2(n\alpha/2) \\ &\quad - V_2 \cos(n\alpha/2)\cos(n\beta/2)\cos(n\delta) \Big] \end{aligned} \tag{10}$$

The mismatch order reactive power can be expressed as:

$$Q_{m\neq n} = V_m I_n = \sum_{n=1,3,5,..} \frac{8V_1\sqrt{A^2+B^2}}{mn^2\pi^2\omega_0 L}\cos(m\alpha/2) \quad (11)$$

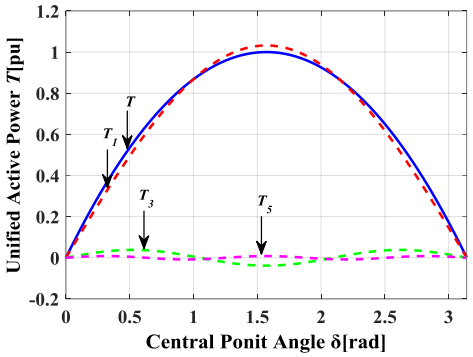

(a)

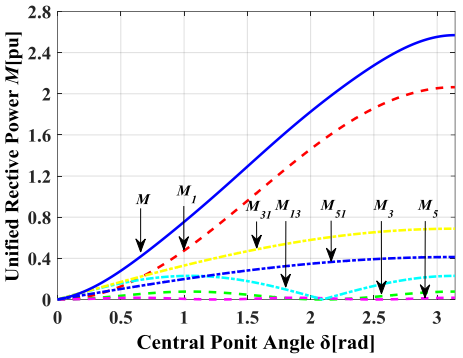

(b)

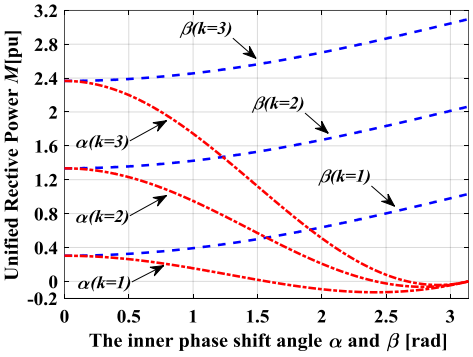

(c)

Fig. 4. (a)The active power distribution with respect to the central point angle δ.(b) The reactive power distribution with respect to the central point angle δ.(c) The reactive power distribution with respect to α, β, and k.

Similarly, both reactive power components are normalized with P_N as:

$$\begin{cases} M_{m=n} = \sum_{n=1,3,5,..} \frac{32\cos(n\alpha/2)}{n^3\pi^3 V_2}\left[V_1\cos(n\alpha/2) - V_2\cos(n\beta/2)\cos(n\delta)\right] \\ M_{m\neq n} = \sum_{m,n=1,3,5,..} \frac{32\sqrt{A^2+B^2}}{mn^2\pi^3 V_2}\cos(m\alpha/2) \end{cases} \quad (12)$$

Fig. 4(b) plots the relationship between the normalized reactive power and angle δ. M represents the unified overall reactive power, while M_1, M_3, M_5 are the fundamental, third order and fifth order component of the unified reactive power. M_{31}, M_{51} are the mismatch order reactive power components which are caused by the fundamental current combined with third and fifth order voltage. Specifically, M_{13} is the mismatch order reactive power component generated by the fundamental voltage and third order current. It can be seen that the reactive power caused by the fundamental current such as M_1, M_{31}, M_{51} are increasing along with the rising of the angle δ. Since the fundamental reactive power shows the largest amplitude during all the components, the whole reactive power can be basically represented by the first order harmonic component [37].

The relationship of the unified reactive power varied with primary and secondary inner phase shift angle α and β are shown in Fig. 4(c) when outer phase shift angle $\delta=\pi/4$. The voltage conversion ratio is defined as "$k= V_1/V_2$". Fig.4 illustrates the case of "$k \geq 1$" and the case "$k < 1$" can be analyzed similarly. It's clearly that higher inner phase shift angle β and k will lead to larger reactive power. For the variable α, higher k will cause higher initial reactive power. The reactive power is initially decreasing along with the increasing α below the zero, and then increasing to the zero when "$\alpha=\pi$". It shows that the reactive power could reach zero twice in the whole α changing region.

III. Reactive Power Optimal Control Strategy

A. Optimal Control Strategy to Reduce Reactive Power

From Fig. 4(a) and (b), the active power is symmetry around $\delta = \pi/2$, while the reactive power is monotonously increased with δ. In order to achieve the minimum reactive power, the central point angle needs to be strictly limited in the $\delta \in [0, \pi/2]$. Besides, the normalized first order components of the active and reactive power from (10) are expressed as:

$$\begin{cases} T_1 = \frac{32}{\pi^3}\cos(\alpha/2)\cos(\beta/2)\sin(\delta) \\ M_1 = \frac{32}{\pi^3 V_2}\cos(n\alpha/2)\left[V_1\cos(n\alpha/2) - V_2\cos(n\beta/2)\cos(n\delta)\right] \end{cases} \quad (13)$$

According to above analysis in section II, the amplitude of the fundamental component is taking charge of the active and reactive power. So fundamental components T_1 and M_1 can be used to represent the total active and reactive power in the optimization algorithm. In order to obtain the minimum reactive power with required active power, the Lagrange multiplier method (LMM) is used, which can be described as:

$$L = M_1 + \lambda\left(T_1 - T_{1,0}\right) \quad (14)$$

where L is the Lagrangian function, λ is the Lagrangian multiplier , the $T_{1,0}$ is the required active power. From the (13)-(15), the LLM method needs to follow the condition below:

$$\begin{cases}\dfrac{\partial L}{\partial \alpha}=0,\dfrac{\partial L}{\partial \beta}=0,\dfrac{\partial L}{\partial \delta}=0\end{cases} \tag{15}$$

The result of the LLM is the boundary condition for minimum reactive power operation. So the result of the (15) can be rewritten as:

$$\begin{cases}\beta=0\\ \delta=\arccos\left(\dfrac{1}{2k\cos\left(\dfrac{\alpha}{2}\right)}\right)\end{cases} \tag{16}$$

The (16) is the LLM boundary condition for achieving minimum reactive power, by taking (16) into (8), the active power for proposed control can be expressed as:

$$T_1=\frac{32}{\pi^3}\cos\left(\frac{\alpha}{2}\right)\sqrt{1-\left[1\Big/\left(2k\cos\left(\frac{\alpha}{2}\right)\right)\right]^2} \tag{17}$$

Due to limitation of the trigonometric function in the (16) and (17), it requires

$$1-\left[1\Big/2k\cos\left(\frac{\alpha}{2}\right)\right]^2\geq 0 \tag{18}$$

So the valid range for proposed control is

$$k\geq\frac{1}{2}\,||\,\alpha\in\left[0,2\arccos\left(1/2k\right)\right] \tag{19}$$

In this paper, we assume *k>1*, so the OPS control is valid in all voltage conversion ratio condition. Then, in order to gain the relationship between independence variable and active power, the inner phase shift α and normalized active power T_1 can be written as:

$$\alpha=2\arccos\left(\sqrt{\left(\pi^3T_1/32\right)^2+\left(1/2k\right)^2}\right) \tag{20}$$

And the valid range of the T_1 can be expressed as:

$$T_1\in\left[0,\frac{32}{\pi^3}\sqrt{1-\frac{1}{4k^2}}\right] \tag{21}$$

From the (21), it can be seen that *k* determines the maximum value of the active power. In this paper, we assume *k*>1. For the smallest condition such as *k*=1, the maximum value $T_{1,\max}\approx 0.92$, which can be generally regarded as covering all load ranges with tolerable error. Furthermore, higher *k* will lead to larger maximum active power. So OPS control can ensure the maximum power transmission ability like the SPS control.

According to the (20), the primary inner phase shift α is inversely proportional to the active power T_1 for any *k* value. The maximum α value is "$\alpha=2\arccos\left(1/2k\right)$" when $T_1=0$, while the minimum value of α is equal to the zero. Because the other control dimensions are all related to the the primary inner phase shift α, α can be seen as the independent variable in OPS control. Then, the output of the PI controller, which is *p**, can be used to directly control the primary inner phase shift α and replace the active power reference $T_{1,0}$ in the control loop. The expression for three variables can be expressed as:

$$\begin{cases}\alpha=2\arccos\left(1/2k\right)\left(1-p^*\right)\\ \beta=0\\ \delta=\arccos\left(1\Big/\left(2k\cos\left(\alpha/2\right)\right)\right)\end{cases} \tag{22}$$

B. Comparison analysis of the OPS

Fig. 5(a) shows the comparison analysis among the different phase shift control methods under the unified reactive power *M* with respect to the unified power *T*. The EPS1 is for the $\alpha=\pi/3$, $\beta=0$ EPS2 is for $\alpha=\pi/2$, $\beta=0$, the DPS is for $\alpha=\pi/3$, $\beta=\pi/3$, and the SPS is for $\alpha=0$, $\beta=0$. It clearly indicates that the higher active power will lead to higher reactive power for all control methods, while the EPS1, EPS2, DPS, and OPS have dramatically lower reactive power than that of the SPS control. The comparison among all control methods shows that the inner phase shift angle α and β will lead to smaller maximum transmission power than those of the SPS and OPS control.

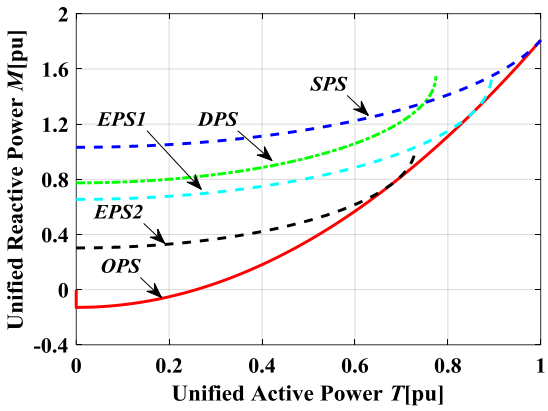

(a)

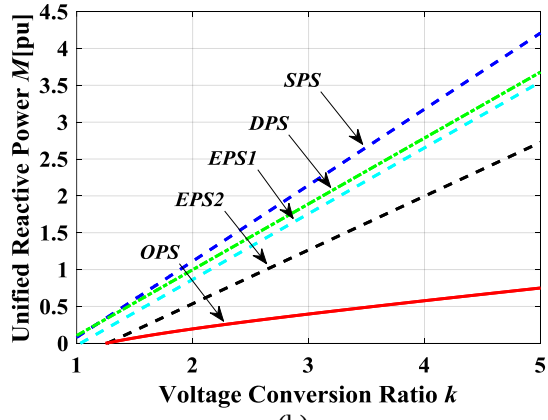

(b)

Fig. 5. (a)The reactive power of DAB varied with unified active power *T* when *k*=2. (b) The reactive power of DAB varied with voltage conversion ratio *k*.

Comparison among the EPS1, EPS2, and DPS show the larger primary inner phase shift angle α can generate lower reactive power under the same transmission active power, and secondary inner phase shift angle β in the DPS control show negative influence on the reducing reactive power and maximum transmission power. For all control methods in this figure, the OPS control method has the lowest reactive power and can nearly cover all load region. Fig. 5. (b) plots the reactive power varied with different voltage conversion ratio k. It indicates reactive power for all control mode will be larger at the higher k. The difference is that SPS, EPS, and DPS are linearly increase, while the rise of reactive power is much slower under OPS control. It means the OPS has better performance in the higher k condition.

C. Establishment of conduction power loss model

1) Switches conduction loss: The conduction loss of switches can be divided into two categories: the power dissipated on the IGBT P_{sw} and the power dissipated on anti-parallel diodes P_D. In fact, due to the difference of the P_{sw} and P_D is not obvious [28], in order to simplify the calculation of the conduction power losses, the saturation voltage of the IGBT $V_{CE}(sat)$ is assumed equal to the diode forward voltage V_f. The total conduction power loss of switches can be expressed as

$$P_{CON\_SW} = P_{SW} + P_D = 2V_{CE}(Sat) \times I_{L,Rms} \tag{23}$$

where P_{CON_SW}, P_{sw} and P_D represent the total switch conduction loss, IGBT conduction loss and anti-parallel diode loss. $V_{CE}(sat)$ is the IGBT on-state saturation voltage, and $I_{L,\ Rms}$ is the root-mean-square (RMS) value of the inductor current. The above equation could approximately estimate the total dissipated power on power switches.

2) Transform conduction loss: The transformer power loss consists of copper loss and iron loss or core losses [39]. The copper loss is defined by the power dissipated on winding resistance R_{Cu}. Based on above analysis about the operation principle of the DAB converter, the inductor current always flows through the transformer. So the copper losses of the transformer can be calculated by

$$P_{Cu} = R_{Cu} \times I_{L,Rms}^2 \tag{24}$$

where P_{Cu} is the transformer copper loss, R_{Cu} is the winding resistance, and $I_{L,RMS}$ is the RMS value of the inductor current.

The iron loss or core loss on the transformer is very complicated because it is associated with the material of the magnetic core, the operation frequency, the core magnetic flux, the total core volume, the excitation voltage waveform, and the operation temperature. Here, the transformer is considered with fundamental sinusoidal voltage excitation, so the Steinmetz equation [40] can be used to estimate the core loss as:

$$P_{Core} = C_m f_s^{\alpha} \hat{B}^2 \tag{25}$$

where f_s is the switching frequency (also the excitation frequency), $\hat{B}$ is the peak magnetic flux density, and C_m, α, β are the empirical parameters. According to the previous study [6], the peak magnetic flux density can be expressed by

$$\hat{B} = V_2 / (4Nf_s \times A_{Core}) \tag{26}$$

where N is the turns ratio of the transformer, V_2 is the secondary side terminal voltage, f_s is the switching frequency and A_{Core} is the cross sectional area of the core.

According to (25) and (26), it is clear that the core loss P_{Core} is only related to the secondary side terminal voltage V_2, not the inductor current, which indicates that the core losses is maintained constant when the voltage V_2 keeps fixed for specific applications.

3) Overall conduction loss model of the DAB converter: Based on the above analysis from (23) to (26), the overall conduction loss of the DAB converter can be written as

$$P_{Cond} = P_{Con\_SW} + P_{Cu} + P_{Core} = 2V_{CE}(Sat) \times I_{L,Rms} + R_{Cu} \times I_{L,Rms}^2 + P_{Core} \tag{27}$$

Based on the equations (25) and (26), P_{Core} is constant within fixed terminal voltage, so the overall conduction loss is decided by the RMS value of the inductor current. According to the above analysis on section II, the RMS of the inductor current can be calculated by

$$I_{Rms\_L} = \frac{\sqrt{P^2 + Q^2}}{V_{B1\_Rms}} \tag{28}$$

where the RMS value of the primary side bridge voltage is

$$V_{B1\_Rms} = \sqrt{\sum_{n=1,3,5,..} \left[\frac{2\sqrt{2}V_1}{n\pi} \cos(n\alpha/2) \right]} \tag{29}$$

Expression (28) indicates that the reduction of the reactive power with specifying active power will lead to less RMS value of the inductor current, which ensure the conduction loss reduction. Fig.6 illustrates the RMS inductor current with different control algorithms. It indicates the OPS has the lowest RMS current, which indicates minimum conduction loss on both the switches and transformer.

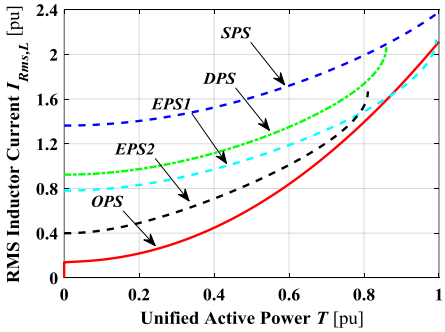

Fig. 6 The RMS inductor current varied with the unified active power by using different control algorithms.

D. Control scheme of the proposed method

The diagram for the control scheme is presented in Fig. 7. The input and output voltage are measured by the voltage sensor LV25-P and then sent into the dSPACE 1104. Then, the PI output p^* and voltage conversion ratio k are

calculated by the optimal control method, and then output the optimal phase shift angle α, β, and δ. After that, those phase shift is transferring to the three switches PWM wave phase shift angle D_1, D_2 and D_3, which can be used to generate the gate signal for switches in DAB converter by the TMS320F28335 DSP board. This control scheme is based on the output of the PI controller, so it only needs two voltage sensors to measure input and output voltage. Compared with the tradition control scheme, which is required to measure input voltage, output voltage, and output current, the proposed control scheme only needs two voltage sensors to measure input and output voltage.

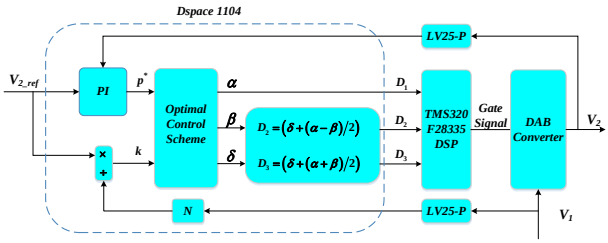

Fig. 7. The control scheme of the proposed method

IV. Harmonic Series Analysis of Soft Switching Region

When the current flows through antiparallel diode of MOSFET or IGBT, which ensures that the switch can turn on at zero voltage. We call this the zero-voltage switching (ZVS). The basic principle to achieve the ZVS soft switching is that the current direction needs be against the voltage direction during the switching instant, while the reverse direction current needs to be larger enough to discharge the switches output capacitor C_{oss}.

Because two switches in the same bridge arm are switched complementarily, their soft switching conditions are same. All switches in the DAB converter can be divided into four pairs: $S_{1,2}$, $S_{3,4}$, $Q_{1,2}$, $Q_{3,4}$. The ZVS boundary conditions are varied with the different operation states (specifically the primary and secondary AC voltage V_{B1} and V_{B2}), which are a function of voltage amplitude, outer phase shift, and inner phase shift. In this paper, we assume the inner phase shift occurs in both arms, so all switch pairs need to be considered. The ZVS condition for each switch pair is judged by the current direction against the terminal voltage direction at the turning-on instant. Furthermore, the reverse direction inductor current at the switching instant must be greater than the minimum discharge current I_{L_min}. So the boundary conditions for those switch pairs are expressed by:

$$\begin{aligned} S_{3,4} &: I_L(\omega_0 t = \frac{\alpha}{2}) \le I_{L\_\min\_p} \\ S_{1,2} &: I_L(\omega_0 t = \pi - \frac{\alpha}{2}) \ge I_{L\_\min\_p} \\ Q_{3,4} &: I_L(\omega_0 t = \delta + \frac{\beta}{2}) \ge I_{L\_\min\_s} \\ Q_{1,2} &: I_L(\omega_0 t = \pi + \delta - \frac{\beta}{2}) \le I_{L\_\min\_s} \end{aligned} \tag{30}$$

where $I_{L\_min\_p}$ is the minimum discharge current for primary side switches and the $I_{L\_min\_s}$ is the minimum discharge current for the secondary bridge. According to the previous research [41], $I_{L\_min\_p}$ and $I_{L\_min\_s}$ can be calculated by

$$I_{L\_\min\_p} = 2\sqrt{V_1 V_2 C_{oss} / L_S} \tag{31}$$

$$I_{L\_\min\_s} = 2\sqrt{V_1 V_2 C_{oss} / N L_S} \tag{32}$$

where V_1 *is* the input terminal voltage, V_2 is the output terminal voltage referred to the primary side, C_{oss} is the output capacitor of switches, L_s is the inductance of the auxiliary inductor, N is the turns ratio of the transformer.

By taking the condition (30) back into the equation (3) and rearranging the expressions, the boundary conditions for soft switching can be rewritten as:

$$\begin{cases} k \ge \dfrac{\sum_{n=1,3,5,..} \frac{4V_2\cos(n\beta/2)}{n^2\pi\omega_0 L}\left[\sin(n\alpha/2)\sin(n\delta)+\cos(n\alpha/2)\cos(n\delta)\right] - I_{L\_\min\_p}}{\sum_{n=1,3,5,..} \frac{4V_2\cos^2(n\alpha/2)}{n^2\pi\omega_0 L}} \\ k \ge \dfrac{\sum_{n=1,3,5,..} \frac{4V_2\cos(n\beta/2)}{n^2\pi\omega_0 L}\left[\sin(n\alpha/2)\sin(n\delta)-\cos(n\alpha/2)\cos(n\delta)\right] - I_{L\_\min\_p}}{\sum_{n=1,3,5,..} -\frac{4V_2\cos^2(n\alpha/2)}{n^2\pi\omega_0 L}} \\ k \le \dfrac{\sum_{n=1,3,5,..} \frac{4V_2\cos(n\beta/2)}{n^2\pi\omega_0 L}\left[\sin(n\delta+n\beta/2)\sin(n\delta)+\cos(n\delta+n\beta/2)\cos(n\delta)\right] - I_{L\_\min\_s}}{\sum_{n=1,3,5,..} \frac{4V_2\cos(n\delta+n\beta/2)\cos(n\alpha/2)}{n^2\pi\omega_0 L}} \\ k \le \dfrac{\sum_{n=1,3,5,..} \frac{4V_2\cos(n\beta/2)}{n^2\pi\omega_0 L}\left[-\sin(n\delta-n\beta/2)\sin(n\delta)-\cos(n\delta-n\beta/2)\cos(n\delta)\right] - I_{L\_\min\_s}}{\sum_{n=1,3,5,..} -\frac{4V_2\cos(n\delta-n\beta/2)\cos(n\alpha/2)}{n^2\pi\omega_0 L}} \end{cases} \tag{33}$$

According to (33), the minimum or maximum voltage conversion ratio k for achieving the ZVS can be calculated by α, β, and δ. The soft switching can be achieved either in the primary bridge when the voltage conversion ratio k is greater than the boundary condition or in the secondary bridge when the voltage conversion ratio k is less than the boundary condition.

Based on (31) and (32), $I_{L\_min\_p}$ and $I_{L\_min\_s}$ are determined by the operation parameters such as the input voltage V_1 and output voltage V_2 combined with the hardware parameters such as output capacitor C_{oss}, auxiliary inductance L_s and transformer turns ratio N. Specifically, these parameters in this design are: V_1=60V, V_2=30V, C_{oss} =350pF, L_s=75μH, and N=2. Thus, the minimum discharge currents are calculated as: $I_{L\_min\_p}$=0.091A and $I_{L\_min\_s}$=0.064A. Fig. 8 plots the influence of minimum discharge currents $I_{L\_min\_p}$ and $I_{L\_min\_s}$ on the ZVS boundaries of the SPS control. The comparison between Fig.8 (a) and (b) indicates that the influence of the discharge current in this paper is insignificant. However, with the increase of $I_{L\_min\_p}$ and $I_{L\_min\_s}$, for instance, 5A and 10A, as illustrated in Fig. 8(c) and (d), respectively, these parameters have a significant influence on the ZVS boundary. It leads to a leftward movement for $S_{3,4}$ boundary line and rightward movement for $Q_{3,4}$ boundary line, which makes the ZVS range narrow.

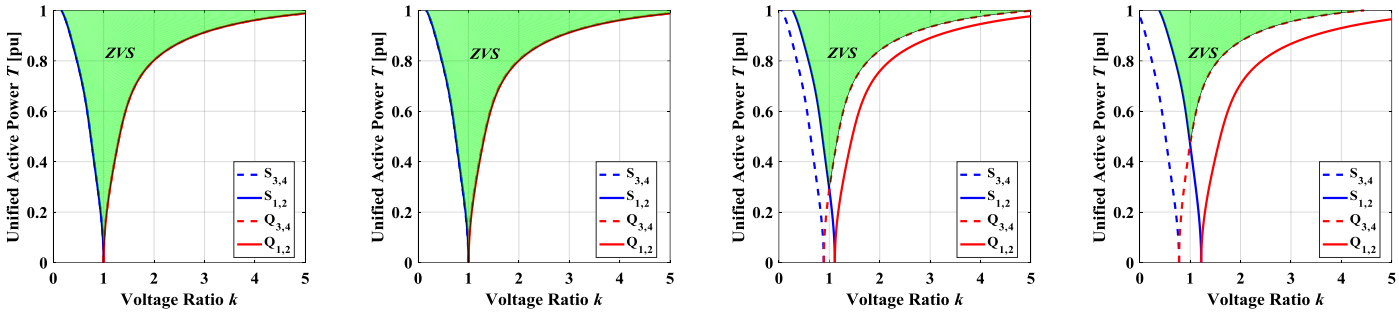

(a) (b) (c) (d)

Fig. 8. ZVS boundaries with SPS control for different minimum discharge currents $I_{L\_min\_p}$ and $I_{L\_min\_s}$.(a) $I_{L\_min\_p}$= 0A and $I_{L\_min\_s}$= 0A. (b) $I_{L\_min\_p}$= 0.091A and $I_{L\_min\_s}$ = 0.064A. (c) $I_{L\_min\_p}$= 5A and $I_{L\_min\_s}$=5A. (d) $I_{L\_min\_p}$= 10A and $I_{L\_min\_s}$=10A.

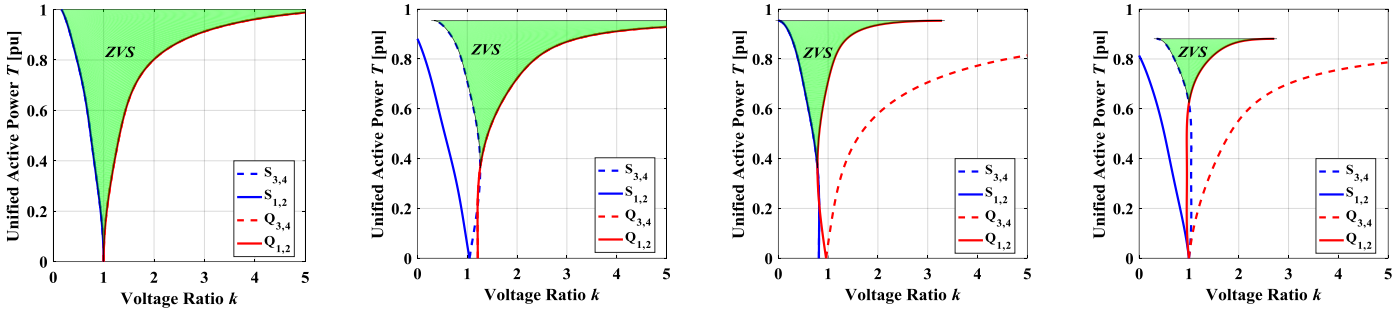

(a) (b) (c) (d)

Fig. 9. (a)ZVS region for α=0 , β=0 and k=2. (b)ZVS region for $\alpha = \pi/4$, β =0 and k=2.(c) ZVS region for α = 0, $\beta = \pi/4$ and k=2.(d) ZVS region for $\alpha = \pi/4$, $\beta = \pi/4$ and k=2.

The ZVS region for each switch pair and the full ZVS area is given in Fig. 9. For the $k>1$ condition, the switch pair $S_{1,2}$ can always achieve ZVS in all load condition, while the voltage ratio limitation for secondary side switches is significantly increasing along with rising active power. Compared with SPS control in Fig. 9 (a), where all primary side or secondary side switches have same boundary conditions. The EPS control in Fig. 9. (b) has different k limitation for the $S_{1,2}$ and $S_{3,4}$ due to the inner phase shift angle α . At the same time, the maximum k for achieving zero-voltage switching of $Q_{1,2,3,4}$ is increasing, which indicates the ZVS on $Q_{1,2,3,4}$ can be easily achieved by using the EPS control. So the EPS control has limited full ZVS region under light load and then extended ZVS region under the heavy load condition. Fig. 9(c) shows the similar result as fig. 9 (b), the inner phase shift β cause separate ZVS boundary for $Q_{1,2}$ and $Q_{3,4}$, but it has smaller ZVS region in the heavy load condition. The DPS control which has the smallest maximum active power and ZVS region is shown in Fig. 9 (d), while the $S_{1,2}$ and $Q_{3,4}$ have similar changes due to the same inner phase angle.

The comparison analysis of Fig. 9 shows the ZVS region is affected by the inner phase shift angle and transmission power. The inner phase shift will narrow a ZVS limitation for one switch pair while extending another switch pair in the same bridge. The increasing transmission power always has a positive influence on the ZVS boundary. The SPS has the largest ZVS area when the k=1 and EPS can improve the ZVS region when the voltage conversion ratio k is higher. Based on the analysis above, it can be seen that the higher voltage conversion ratio k may lead to narrower ZVS region for all switches, so the $k=1$ has the best ZVS performance under SPS.

Compared with the SPS, EPS and DPS control, the ZVS analysis for OPS control in this paper is different. Because the expression of the OPS control method in (22) is related to the voltage conversion ratio k. So it needs to be discussed under different variable k to investigate the ZVS situation. According to Fig. 10 and above analysis, the ZVS region is mainly determined by switch pairs $S_{3,4}$, while the $S_{1,2}$ can be always achieved zero-voltage switching during all load condition when $k>1$. In the same time, the ZVS boundary for the secondary side $Q_{1,2}$ and $Q_{3,4}$ are same due to the none inner phase shift on the secondary side. So the $S_{3,4}$ and $Q_{1,2}$ are used to investigate the ZVS region under OPS control. Fig. 10(a) is the ZVS region for the OPS control. It can be seen that the relationship for the ZVS boundary is obviously different from the traditional phase shift method in Fig. 9 due

to the variable inner phase shift α . Compared with EPS control, the OPS control has a much higher boundary for the $S_{3,4}$. The ZVS boundary is firstly sharply climbing to the peak at T=0.2 due to a large α and increasing unified power p which cause the positive direction reactive power of DAB is reducing to zero at T=0.2. Then, the boundary condition is decreasing to zero due to the reducing α and higher T which causes the zero reactive power is increasing in the negative direction. This tendency is also to follow the reactive power analysis about the OPS control in Fig. 5(a). In the full transmission condition or T=1 condition, the OPS is acting as SPS control which is also confirmed by the ZVS analysis. The ZVS boundary condition for secondary side $Q_{1,2}$ is significantly higher in the light load condition, while has the same condition in the maximum transmission power. By the help of the black line which stands for k in this ZVS analysis, it can be seen that the OPS control can achieve full ZVS control since T=0.6, which is lower than the fixed α EPS control, so the entire ZVS region is extended. The comparison analysis between Fig. 10 (a) and (b) indicate that higher k will lead to larger boundary value for $S_{3,4}$ and $Q_{1,2}$ conducting zero-voltage switching. Although ZVS boundaries for $S_{3,4}$ and $Q_{1,2}$ are higher, the full ZVS is increasing in the higher voltage conversion ratio k, which is dramatically different from the traditional SPS, EPS and DPS control. It proves the OPS control can not only extend overall ZVS region but also can improve the ZVS region in the higher k condition.

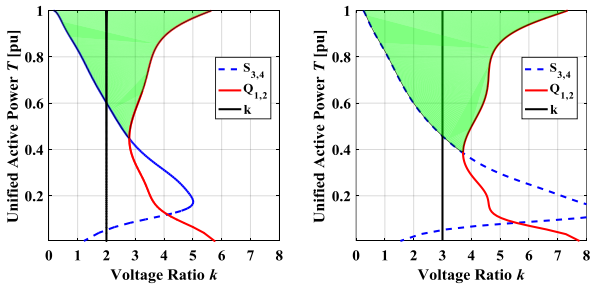

Fig. 10. (a)ZVS region for OPS and k=2. (b) ZVS region for OPS and k=3.

V. Experimental Results

A 200W prototype of the DAB converter was built to verify the effectiveness of the proposed algorithm. Main parameters are shown here: the auxiliary inductor $L=75\mu H$, the switching frequency $f_s=20kHz$, and input voltage $V_1=60V$ and the output voltage refer to the primary side $V_2=30V$, the turns ratio of the transformer $N=2$, so the output terminal voltage $NV_2=60V$.

Fig. 11 shows the comparison of typical waveforms by using the theoretical harmonics analysis and experimental test for different control methods such as SPS, EPS and DPS control. It can be seen that the theoretical waveforms match well with the experimental waveforms for all control methods, which indicates that the harmonicas mathematical analysis adopted in section II is effective.

The experimental comparison results among SPS, EPS under "$\alpha=\pi/3$", and OPS for the heavy-load condition are shown in Fig. 12. It is clear that both OPS and EPS can significantly reduce the additional reactive power or backflow power existed in the SPS control. The main reason is that the reverse direction current in the OPS and EPS control is circulating inside the primary bridge due to the inclusion of an inner phase shift between two active bridge arms. Compared with EPS control with a fixed inner phase shift, the OPS control can adjust its inner phase shift α and reach the optimized operation point, so the OPS can achieve lower backflow power than EPS control, which was proved by Fig. 12(b) and (c). Because the backflow power is a part of the reactive power, the total reactive power can be clearly minimized by the OPS control, which is beneficial for the efficiency improvement.

In the experiment waveforms of Fig. 12, ZVS soft switching conditions for $S_{3,4}$ and $Q_{1,2,3,4}$ with different methods can be also investigated. Since the switch pair $S_{1,2}$ can always achieve ZVS in all load condition, the $S_{3,4}$ is marked by blue dotted line circle, and the $Q_{1,2,3,4}$ is marked by red line circle to show their soft-switching condition. It indicates that both EPS and OPS can achieve fully ZVS soft switching and the OPS has wider ZVS region under the heavy-load condition, which verifies the theoretical analysis in Fig. 9 and 10.

Fig.13 illustrates the experimental results under the light-load condition. It shows that under the OPS can significantly eliminate the backflow power, which will result in low efficiency with the SPS control under the light-load condition. Furthermore, although the SPS and EPS can achieve ZVS for all four primary-side bridge switches $S_{1,2,3,4}$, the OPS can ensure $S_{1,2}$ and $Q_{1,2,3,4}$ turning on with zero-voltage switching, which maintains six switches operated with soft-switching. The experimental results under different conditions prove that OPS can realize the lower reactive power and wider soft switching region under various load conditions, in particular for the light-load condition. As it indicated in Fig. 13, the traditional outer phase shift θ, defined in Fig. 2, is almost equal to zero by using the OPS control. However, the central point outer phase shift is expressed by "$\delta=\theta+(\alpha-\beta)/2$" . So it is larger than zero by considering the inner phase shift angle α. Thus, the transmission power is greater than zero by using the OPS control, which indicates that the traditional outer phase shift θ is not suitable for the 3-level modulated phase shift control.

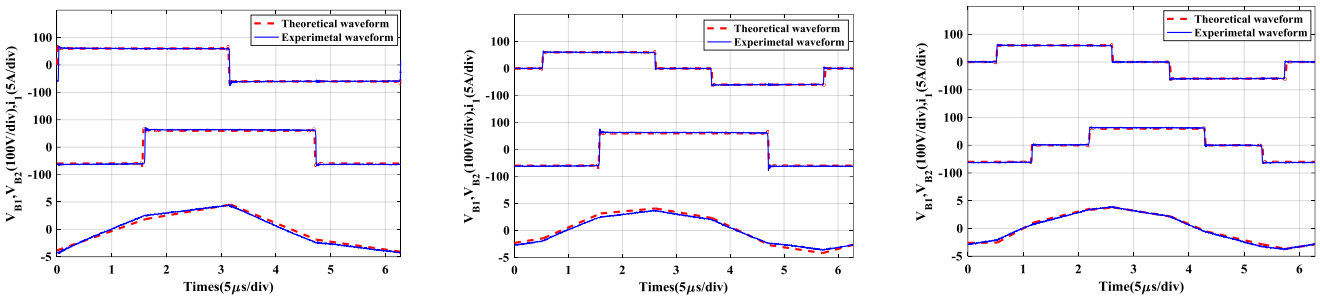

(a) (b) (c)

Fig. 11. Comparison of typical waveforms by using the theoretical harmonics analysis and experimental test for different control methods: (a)SPS. (b)EPS. (c)DPS.

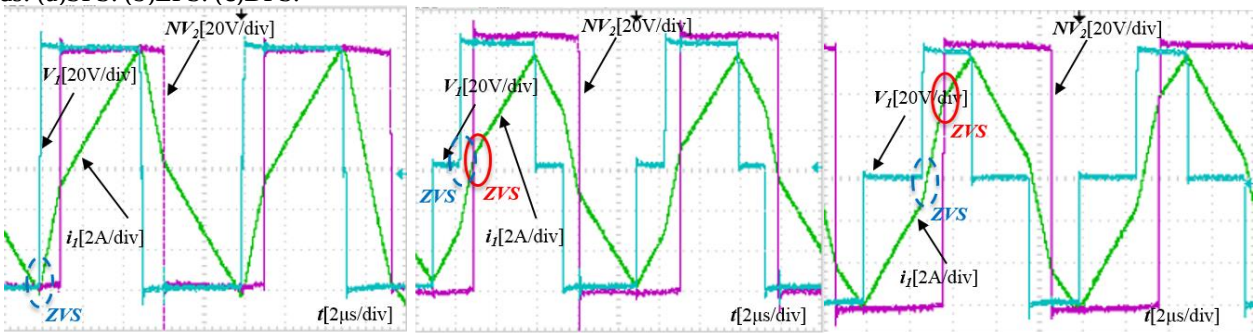

(a) (b) (c)

Fig. 12. (a) Experiment waveform for SPS control with V_1=60 V, NV_2=60 V and P=90 W.(b) Experiment waveform for EPS control with V_1=60 V, NV_2=60 V and P=90 W. (c) Experiment waveform for OPS control with V_1=60 V, NV_2 =60 V and P=90 W.

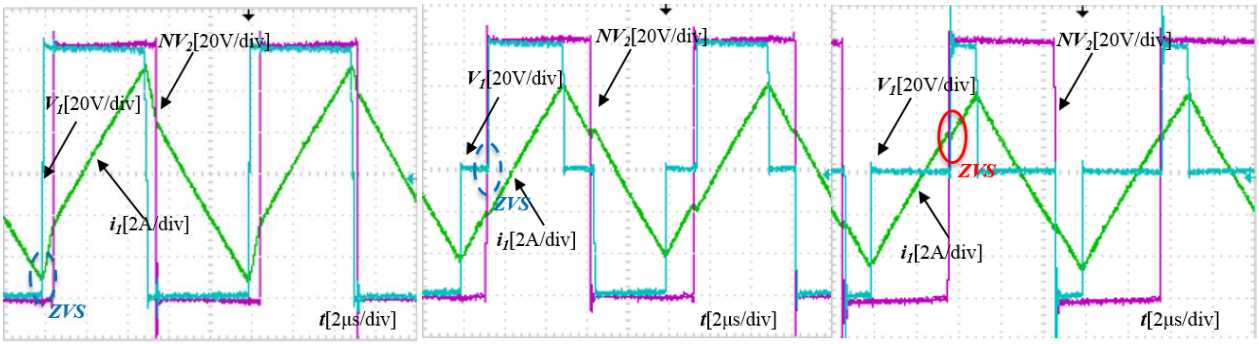

(a) (b) (c)

Fig. 13. (a) Experiment waveform for SPS control with V_1=60 V, NV_2=60 V and P=48 W.(b) Experiment waveform for EPS control with V_1=60 V, NV_2=60 V and P=48 W. (c) Experiment waveform for OPS control with V_1=60 V, NV_2=60 V and P=48 W.

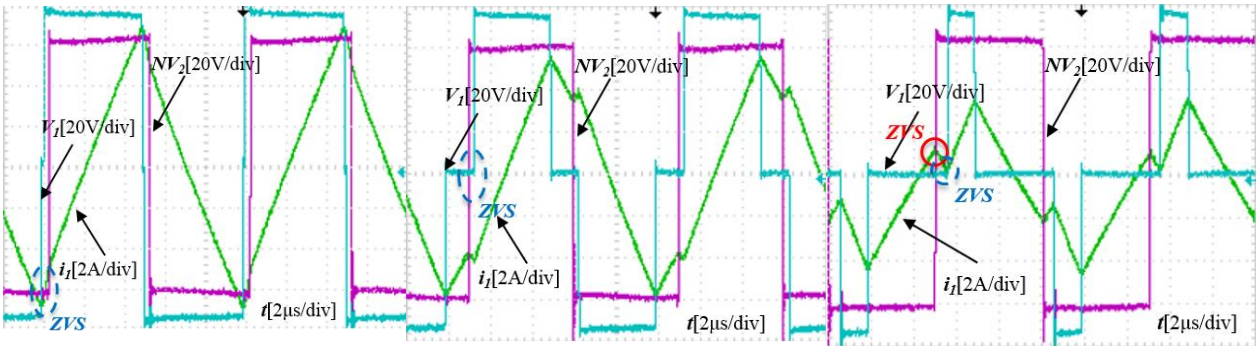

(a) (b) (c)

Fig. 14. (a) Experiment waveform for SPS control with V_1=75 V, NV_2=60 V and P=48 W.(b) Experiment waveform for EPS control with V_1=75 V, NV_2=60 V and P=48 W. (c) Experiment waveform for OPS control with V_1=75 V, NV_2=60 V and P=48 W.

Fig. 14. illustrates the experimental results for different voltage conversion ratio *k*, specifically, the ratio is calculated as 2.5. Compared with the situation of "*k=2*" illustrated in Fig. 13, the backflow power is larger and the ZVS soft-switching region becomes narrower by using the SPS and EPS control, which is consistent with the theoretical analysis conclusion, specifically the higher voltage conversion ratio *k* will result in larger reactive power and narrower ZVS range. However, for different voltage conversion ratios, the OPS can still eliminate the backflow power and achieve fully soft switching. As shown in Fig. 14 (c), the $S_{3,4}$ devices are on the ZVS boundary condition. Furthermore, the current of two devices are equal to zero at this moment. Thus, these two devices also achieve zero-current-switching soft switching under this condition.

Fig. 15(a) shows the reactive power by using different control methods varied with the transmission power. The comparison result indicates that OPS has the lowest reactive power among all control methods. Meanwhile, the curves of EPS and DPS control prove that they can effectively reduce the reactive power. With the same transmission power, EPS has slightly lower reactive power than that of DPS.

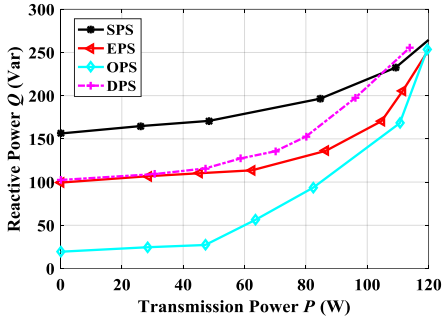

(a)

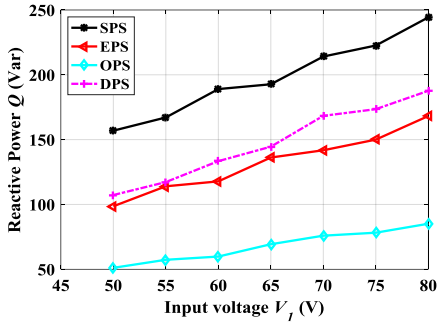

(b)

Fig. 15. (a) Comparison of reactive power *Q* by using different control methods varied with transmission power *P* when V_1=60V, NV_2=60V. (b) Reactive power *Q* by using different control methods varied with different input voltage V_1 when NV_2=60V, *P*= 72W.

The comparison result also shows that OPS is the most effective method for the light load condition. When the transmission power *P*=0W, the reactive power by using OPS can reduce reactive power from 156.2 Var of SPS and 99.4 Var of EPS to 19.4 Var. However, when the transmission power increases such as *P*=120W, EPS and OPS show the similar reactive power. This phenomenon verifies the analytic result in Fig. 5(a). In Fig. 15(b), the comparison results of the reactive power among SPS, EPS, DPS, and OPS varied with input voltage V_1 show that the reactive power by using any method is increasing along with the input voltage V_1. Among all control methods, OPS can achieve the lowest reactive power, especially under the condition of larger input voltage V_1 or larger voltage conversion ratio *k*.

The theoretical and experimental harmonics components of the active and reactive power with SPS control is shown in Fig. 16. It is clear that major harmonic components of both active and reactive power are concentrated on the odd-order components, furthermore, the fundamental component shows the highest amplitude among all harmonic components.

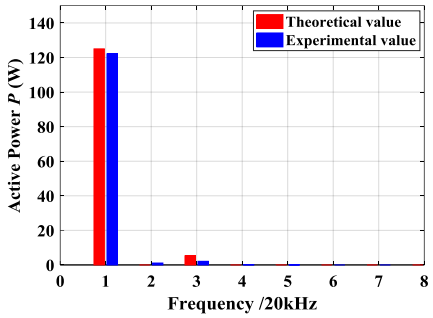

(a)

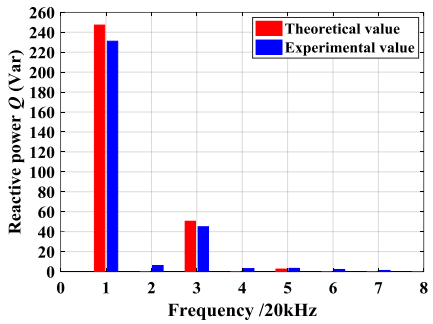

(b)

Fig. 16. (a) Harmonic components of the active power *P* with SPS when V_1=60V, NV_2=60V, *P*=120W. (b) Harmonic components of the reactive power *Q* with SPS when V_1=60V, NV_2=60V, *P*=120W.

The comparison results of the efficiency by using the SPS, EPS, DPS and OPS with respect to the transmission power are shown in Fig. 17(a). It can be seen that the measured efficiencies with all these control methods are increasing along with the transmission power, while OPS control has the highest efficiency for all conditions. Compared with SPS control, both EPS and DPS are effective for the efficiency improvement of the DAB converter. The efficiency with DPS control is slightly lower

than that of EPS for majority conditions, which is in accordance with the previous analysis. It also shows the OPS is the most effective method for the light-load condition, specifically the efficiency is improved from 81.1% of SPS to 86.8% under the light-load condition. With the increasing of the transmission power, the efficiency by using OPS is high up to 95.5% under "P=120W".

In order to investigate the influence of the voltage conversion ratio k, the efficiencies of the DAB converter by using the SPS, EPS DPS and OPS control under different input voltage V_1 are also recorded. The output voltage is regulated at a constant value of 60V and the transmission power is fixed as 72W for all conditions. The efficiency comparison by using the SPS, EPS, DPS and OPS varied with the input voltage V_1 is illustrated in Fig. 17(b). It shows that the increase of the input voltage leads to the rapid decrease of the efficiency by using the SPS control, while the decreasing speed of the efficiency by using the EPS and OPS is much slower. Compared with the efficiency differences among EPS, DPS and OPS control for different input voltage, the efficiency difference is largest for the largest input voltage condition "V_1=80V", which indicates the OPS can gain higher efficiency improvement with higher voltage conversion ratio k. Based on those figures and experimental waveforms, the conclusion can be drawn that OPS control can effectively reduce the reactive power and improve the efficiency especially for the light-load and high-voltage-conversion condition.

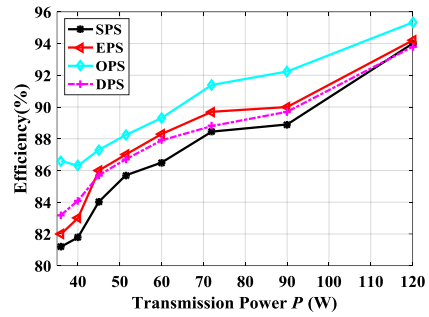

(a)

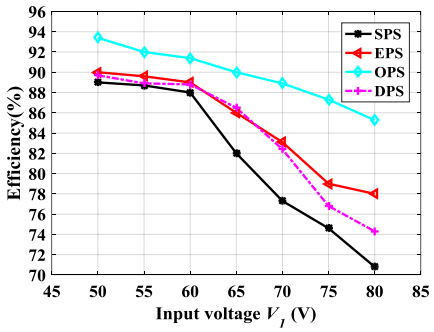

(b)

Fig. 17. (a) Efficiency comparison of different control methods varied with transmission power P when V_1=60V, NV_2=60V. (b) Efficiency comparison of different control methods varied with input voltage V_1 when NV_2=60V, P= 72W.

VI. Conclusion

A novel reactive power reduction method under 3-level modulated phase shift control is proposed in this paper. According to the universal fundamental reactive power expression from harmonics analysis and the Lagrange multiplier method (LMM), the reactive power distributions by using different control methods can be analyzed for all load range, while their soft switching ranges can also be specified. Then, the reactive power distributions among SPS, EPS, and DPS have been compared, which shows that the OPS can guarantee the minimum reactive power as well as the larger ZVS range for various load and voltage conversion ratio conditions. The reduction of the reactive power and extension of soft switching range can dramatically decrease both conduction and switching losses of the DAB and improve its overall efficiency. Besides, the reactive-power oriented closed-loop control is proposed. The research shows that the optimal algorithm by using the harmonics analysis can significantly simplify the digital implemented on the microcontroller because it avoids multiple modes selection for various voltage conversion ratios or transmission power in the traditional piecewise time domain algorithm. Experimental results on the DAB porotype have been illustrated and verified the effectiveness of this proposed method.

VII. ACKNOWLEDGEMENT

This work was supported by the Research development fund of XJTLU (RDF-14-02-03), the Jiangsu Science and Technology Programme (BK20161252), the Visiting Scholarship of State Key Laboratory of Power Transmission Equipment & System Security and New Technology (2007DA10512716414), and the National Nature Science Foundation of China (51407145).

References

[1] B. Zhao, Q. Song, W. Liu, and Y. Sun, "Overview of Dual-Active-Bridge Isolated Bidirectional DC-DC Converter for High-Frequency-Link Power-Conversion System," IEEE Transactions on Power Electronics, vol. 29, pp. 4091-4106, 2014.

[2] H. Wen, and B. Su "Reactive Power and Soft-Switching Capability Analysis of Dual-Active-Bridge DC-DC Converters with Dual-Phase-Shift Control," Journal of Power Electronics, vol. 15, pp. 18-30, 2015.

[3] J. Riedel, D. G. Holmes, B. P. McGrath and C. Teixeira, "ZVS Soft Switching Boundaries for Dual Active Bridge DC–DC Converters Using Frequency Domain Analysis," IEEE Transactions on Power Electronics, vol. 32, pp. 3166-3179, 2017.

[4] C. Mi, H. Bai, C. Wang, and S. Gargies, "Operation, design and control of dual H-bridge-based isolated bidirectional DC–DC converter," IET Power Electronics, vol. 1, p. 507, 2008.

[5] Y. Xie, J. Sun, and J. S. Freudenberg, "Power Flow Characterization of a Bidirectional Galvanically Isolated High-Power DC/DC Converter Over a Wide Operating Range," IEEE Transactions on Power Electronics, vol. 25, pp. 54-66, 2010.

[6] F. Krismer and J. W. Kolar, "Accurate Power Loss Model Derivation of a High-Current Dual Active Bridge Converter for an Automotive Application," IEEE Transactions on Industrial Electronics, vol. 57, pp. 881-891, 2010.

[7] S. Inoue and H. Akagi, "A Bidirectional Isolated DC-DC Converter as a Core Circuit of the Next-Generation Medium-Voltage Power

Conversion System," IEEE Transactions on Power Electronics, vol. 22, pp. 535-542, 2007.
[8] S. Inoue and H. Akagi, "A Bidirectional DC-DC Converter for an Energy Storage System With Galvanic Isolation," IEEE Transactions on Power Electronics, vol. 22, pp. 2299-2306, 2007.
[9] H. Bai, C. C. Mi, and S. Gargies, "The Short-Time-Scale Transient Processes in High-Voltage and High-Power Isolated Bidirectional DC-DC Converters," IEEE Transactions on Power Electronics, vol. 23, pp. 2648-2656, 2008.
[10] Y. Shi, R. Li, Y. Xue, and H. Li, "Optimized Operation of Current-Fed Dual Active Bridge DC-DC Converter for PV Applications," IEEE Transactions on Industrial Electronics, vol. 62, pp. 6986-6995, 2015.
[11] M. Jafari, Z. Malekjamshidi, and J. G. Zhu, "Analysis of operation modes and limitations of dual active bridge phase shift converter," in 2015 IEEE 11th International Conference on Power Electronics and Drive Systems, 2015, pp. 393-398.
[12] A. S. Babokany, M. Jabbari, G. Shahgholian, and M. Mahdavian, "A review of bidirectional dual active bridge converter," in Electrical Engineering/Electronics, Computer, Telecommunications and Information Technology (ECTI-CON), 2012 9th International Conference on, 2012, pp. 1-4.
[13] L. Xue, Z. Shen, D. Boroyevich, P. Mattavelli, and D. Diaz, "Dual Active Bridge-Based Battery Charger for Plug-in Hybrid Electric Vehicle With Charging Current Containing Low Frequency Ripple," IEEE Transactions on Power Electronics, vol. 30, pp. 7299-7307, 2015.
[14] H. Bai, Z. Nie, and C. C. Mi, "Experimental Comparison of Traditional Phase-Shift, Dual-Phase-Shift, and Model-Based Control of Isolated Bidirectional DC-DC Converters," IEEE Transactions on Power Electronics, vol. 25, pp. 1444-1449, 2010.
[15] H. Bai and C. Mi, "Eliminate Reactive Power and Increase System Efficiency of Isolated Bidirectional Dual-Active-Bridge DC-DC Converters Using Novel Dual-Phase-Shift Control," IEEE Transactions on Power Electronics, vol. 23, pp. 2905-2914, 2008.
[16] B. Zhao, Q. Song, and W. Liu, "Power Characterization of Isolated Bidirectional Dual-Active-Bridge DC-DC Converter With Dual-Phase-Shift Control," IEEE Transactions on Power Electronics, vol. 27, pp. 4172-4176, 2012.
[17] B. Zhao, Q. Yu, and W. Sun, "Extended-Phase-Shift Control of Isolated Bidirectional DC-DC Converter for Power Distribution in Microgrid," IEEE Transactions on Power Electronics, vol. 27, pp. 4667-4680, 2012.
[18] G. Oggier, G. O. Garc, x00Ed, and A. R. Oliva, "Modulation strategy to operate the dual active bridge DC-DC converter under soft switching in the whole operating range," IEEE Transactions on Power Electronics, vol. 26, pp. 1228-1236, 2011.
[19] A. K. Jain and R. Ayyanar, "Pwm control of dual active bridge: Comprehensive analysis and experimental verification," IEEE Transactions on Power Electronics, vol. 26, pp. 1215-1227, 2011.
[20] H. Wen, B. Su, and W. Xiao, "Design and performance evaluation of a bidirectional isolated dc-dc converter with extended dual-phaseshift scheme," IET Power Electronics, vol. 6, pp. 914-924, 2013.
[21] K. Wu, C. W. d. Silva, and W. G. Dunford, "Stability Analysis of Isolated Bidirectional Dual Active Full-Bridge DC-DC Converter With Triple Phase-Shift Control," IEEE Transactions on Power Electronics, vol. 27, pp. 2007-2017, 2012.
[22] H. Wen and W. Xiao, "Bidirectional dual-active-bridge DC-DC converter with triple-phase-shift control," in Applied Power Electronics Conference and Exposition (APEC), 2013 Twenty-Eighth Annual IEEE, 2013, pp. 1972-1978.
[23] Y. A. Harrye, K. H. Ahmed, and A. A. Aboushady, "Reactive power minimization of dual active bridge DC/DC converter with triple phase shift control using neural network," in 2014 International Conference on Renewable Energy Research and Application (ICRERA), 2014, pp. 566-571.
[24] H. Wen, W. Xiao, and B. Su, "Nonactive Power Loss Minimization in a Bidirectional Isolated DC-DC Converter for Distributed Power Systems," IEEE Transactions on Industrial Electronics, vol. 61, pp. 6822-6831, 2014.
[25] B. Zhao, Q. Song, W. Liu, and W. Sun, "Current-Stress-Optimized Switching Strategy of Isolated Bidirectional DC-DC Converter With Dual-Phase-Shift Control," IEEE Transactions on Industrial Electronics, vol. 60, pp. 4458-4467, 2013.
[26] B. Feng, Y. Wang, and J. Man, "A novel dual-phase-shift control strategy for dual-active-bridge DC-DC converter," in IECON 2014 - 40th Annual Conference of the IEEE Industrial Electronics Society, 2014, pp. 4140-4145.
[27] N. Hou, W. Song, and w. m, "Minimum-Current-Stress Scheme of Dual Active Bridge DC-DC Converter With Unified-phase-shift Control," IEEE Transactions on Power Electronics, vol. PP, pp. 1-1, 2016.
[28] B. Zhao, Q. Song, and W. Liu, "Efficiency Characterization and Optimization of Isolated Bidirectional DC-DC Converter Based on Dual-Phase-Shift Control for DC Distribution Application," IEEE Transactions on Power Electronics, vol. 28, pp. 1711-1727, 2013.
[29] B. Zhao, Q. Song, W. Liu, and Y. Sun, "Overview of Dual-Active-Bridge Isolated Bidirectional DC-DC Converter for High-Frequency-Link Power-Conversion System," IEEE Transactions on Power Electronics, vol. 29, pp. 4091-4106, 2014.
[30] A. Rodr, A. Vazquez, D. Lamar, et al., "Different Purpose Design Strategies and Techniques to Improve the Performance of a Dual Active Bridge With Phase-Shift Control," IEEE Transactions on Power Electronics, vol. 30, pp. 790-804, 2015.
[31] F. Krismer and J. W. Kolar, "Accurate Small-Signal Model for the Digital Control of an Automotive Bidirectional Dual Active Bridge," IEEE Transactions on Power Electronics, vol. 24, pp. 2756-2768, 2009.
[32] J. Riedel, C. Teixeira, D. G. Holmes, and B. P. McGrath, "Identification of ZVS soft switching boundaries for three-phase dual active bridge converters using harmonic analysis," in Power Electronics and Applications (EPE'15 ECCE-Europe), 2015 17th European Conference on, 2015, pp. 1-10.
[33] D. Costinett, R. Zane, and D. Maksimovic, "Discrete time modeling of output disturbances in the dual active bridge converter," in 2014 IEEE Applied Power Electronics Conference and Exposition - APEC 2014, 2014, pp. 1171-1177.
[34] F. Krismer and J. W. Kolar, "Closed Form Solution for Minimum Conduction Loss Modulation of DAB Converters," IEEE Transactions on Power Electronics, vol. 27, pp. 174-188, 2012.
[35] G. G. Oggier, G. O. Garc, and A. R. Oliva, "Switching Control Strategy to Minimize Dual Active Bridge Converter Losses," IEEE Transactions on Power Electronics, vol. 24, pp. 1826-1838, 2009.
[36] B. Zhao, Q. Song, W. Liu, and Y. Sun, "A Synthetic Discrete Design Methodology of High-Frequency Isolated Bidirectional DC/DC Converter for Grid-Connected Battery Energy Storage System Using Advanced Components," IEEE Transactions on Industrial Electronics, vol. 61, pp. 5402-5410, 2014.
[37] B. Zhao, Q. Song, W. Liu, G. Liu, and Y. Zhao, "Universal High-Frequency-Link Characterization and Practical Fundamental-Optimal Strategy for Dual-Active-Bridge DC-DC Converter Under PWM Plus Phase-Shift Control," IEEE Transactions on Power Electronics, vol. 30, pp. 6488-6494, 2015.
[38] H.Shi, H. Wen and J. Chen, "Reactive power reduction method based on harmonics analysis for dual active bridge converters with 3-level modulated phase-shift control," in IEEE International Conference on Power Electronics, Drives and Energy Systems (PEDES), 2016, pp. 1-6.
[39] Y. Han and Y. F. Liu, "A Practical Transformer Core Loss Measurement Scheme for High-Frequency Power Converter," IEEE Transactions on Industrial Electronics, vol. 55, pp. 941-948, 2008.
[40] J. Reinert, A. Brockmeyer, and R. W. A. A. D. Doncker, "Calculation of losses in ferro- and ferrimagnetic materials based on the modified Steinmetz equation," IEEE Transactions on Industry Applications, vol. 37, pp. 1055-1061, 2001.
[41] S. Zhiyu, R. Burgos, D. Boroyevich, and F. Wang, "Soft-switching capability analysis of a dual active bridge dc-dc converter," in 2009 IEEE Electric Ship Technologies Symposium, 2009, pp. 334-339.

Haochen Shi was born in Hubei, China, in 1992. He received the B.S. degree from the Department of Electrical Engineering, China Three Gorge University, Yichang, China, in 2014. He received the M.Eng. degree from the Department of Electrical Engineering, University of Leicester, Leicester, UK, in 2015. He is currently working toward the Ph.D. degree at the University of Liverpool, U.K. His current research interests include bidirectional dc-dc converter, electrical vehicles, and renewable power conversion system.

Huiqing Wen (M'13) received his B.S. and M.S. degrees in Electrical Engineering from Zhejiang University, Hangzhou, China, in 2002 and 2006, respectively; and his Ph.D. degree in Electrical Engineering from the Chinese Academy of Sciences, Beijing, China, in 2009. From 2009 to 2010, he was an Electrical Engineer working in the Research and Development Center, GE (China) Co., Ltd., Shanghai, China. From 2010 to 2011, he was an Engineer at the China Coal Research Institute, Beijing, China. From 2011 to 2012, he was a Postdoctoral Fellow at the Masdar Institute of Science and Technology, Abu Dhabi, United Arab Emirates. Currently, he is presently working as an Associate Professor at the Xi'an Jiaotong-Liverpool University, Suzhou, China. His current research interests include bidirectional DC-DC converters, power electronics in flexible AC transmission applications, electrical vehicles, and high-power, three-level electrical driving systems.

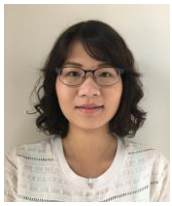

Jie Chen was born in Yunnan, China in 1994. She received the B.S. degree from the Department of Electrical Engineering, Xi'an Jiaotong-Liverpool University, Suzhou, China, in 2016. She is currently an assistant officer in the Department of Electrical Engineering, Xi'an Jiaotong-Liverpool University, Suzhou, China. Her current research interests include bidirectional dc-dc converter and high power multi-level converters.

Yihua Hu (M'13-SM'15) received his B.S. degree in Electrical Motor Drives, and his Ph.D. degree in Power Electronics and Drives, from the China University of Mining and Technology, Jiangsu, China, in 2003 and 2011, respectively. From 2011 to 2013, he was a Postdoctoral Fellow in the College of Electrical Engineering, Zhejiang University, Hangzhou, China. From November 2012 to February 2013, he was an Academic Visiting Scholar in the School of Electrical and Electronic Engineering, Newcastle University, Newcastle upon Tyne, ENG, UK. From 2013 to 2015, he worked as a Research Associate in the Power Electronics and Motor Drive Group, University of Strathclyde, Glasgow, SCT, UK. He is presently working as a Lecturer in the Department of Electrical Engineering and Electronics, University of Liverpool, Liverpool, ENG, UK. He has published more than 36 peer reviewed technical papers in leading journals. His current research interests include PV generation systems, power electronics converters and control, and electrical motor drives.

Lin Jiang (M'00) received his B.S. and M.S. degrees in Electrical Engineering from the Huazhong University of Science and Technology, Wuhan, China, in 1992 and 1996, respectively; and his Ph.D. degree in Electrical Engineering from the University of Liverpool, Liverpool, ENG, UK, in 2001. He is presently working as a Reader of Electrical Engineering at the University of Liverpool. His current research interests include the optimization and control of smart grids, electrical machines, power electronics and renewable energy.

Guipeng Chen (S'16) received the B.E.E. and Ph.D. degrees from the Department of Electrical Engineering, Zhejiang University, Hangzhou, China, in 2011 and 2017, respectively. He is currently working as a Postdoc at the School of Aerospace Engineering, Xiamen University, Xiamen, China.

His current research interests include topology derivation of DC-DC converters and fault-tolerant converters.